

Cyst-X: AI-Powered Pancreatic Cancer Risk Prediction from Multicenter MRI in Centralized and Federated Learning

Hongyi Pan¹, Gorkem Durak¹, Elif Keles¹, Deniz Seyithanoglu², Zheyuan Zhang¹, Alpay Medetalibeyoglu², Halil Ertugrul Aktas¹, Andrea Mia Bejar¹, Ziliang Hong¹, Yavuz Taktak², Gulbiz Dagoglu Kartal², Mehmet Sukru Erturk², Timurhan Cebeci², Maria Jaramillo Gonzalez³, Yury Velichko¹, Lili Zhao⁴, Emil Agarunov⁵, Federica Proietto Salanitri⁶, Concetto Spampinato⁶, Pallavi Tiwari³, Ziyue Xu⁷, Sachin Jambawalikar⁸, Ivo G. Schoots⁹, Marco J. Bruno¹⁰, Chenchang Huang⁵, Candice Bolan¹¹, Tamas Gonda⁵, Frank H. Miller¹, Rajesh N. Keswani¹², Michael B. Wallace^{11*}, Ulas Bagci^{1*}

¹Machine & Hybrid Intelligence Lab, Department of Radiology, Northwestern University, Chicago, IL, USA.

²Istanbul Faculty of Medicine, Istanbul University, Istanbul, Turkey.

³Department of Biomedical Engineering and Radiology, University of Wisconsin-Madison, Madison, WI, USA.

⁴Department of Preventive Medicine, Northwestern University, Chicago, IL, USA.

⁵Division of Gastroenterology and Hepatology, New York University, New York, NY, USA.

⁶Department of Electrical, Electronic and Computer Engineering, University of Catania, Catania, Italy.

⁷NVIDIA, Bethesda, MD, USA.

⁸Department of Radiology, Columbia University, New York, NY, USA.

⁹Department of Radiology and Nuclear Medicine, Erasmus Medical Center, Rotterdam, Netherlands.

¹⁰Department of Gastroenterology and Hepatology, Erasmus Medical Center, Rotterdam, Netherlands.

¹¹Division of Gastroenterology and Hepatology, Mayo Clinic Florida, Jacksonville, FL, USA.

¹²Department of Gastroenterology and Hepatology, Northwestern University, Chicago, IL, USA.

*Corresponding author(s). E-mail(s): wallace.michael@mayo.edu;
ulas.bagci@northwestern.edu;

Abstract

Pancreatic cancer is projected to become the second-deadliest malignancy in Western countries by 2030, highlighting the urgent need for better early detection. Intraductal papillary mucinous neoplasms (IPMNs), key precursors to pancreatic cancer, are challenging to assess with current guidelines, often leading to unnecessary surgeries or missed malignancies. We present *Cyst-X*, an AI framework that predicts IPMN malignancy using multicenter MRI data, leveraging MRI’s superior soft tissue contrast over CT. Trained on 723 T1- and 738 T2-weighted scans from 764 patients across seven institutions, our models (AUC=0.82) significantly outperform both Kyoto guidelines (AUC=0.75) and expert radiologists. The AI-derived imaging features align with known clinical markers and offer biologically meaningful insights. We also demonstrate strong performance in a federated learning setting, enabling collaborative training without sharing patient data. To promote privacy-preserving AI development and improve IPMN risk stratification, the *Cyst-X* dataset is released as the first large-scale, multi-center pancreatic cysts MRI dataset.

Keywords: IPMN, Pancreatic Cancer, Segmentation, Classification, Federated Learning

1 Introduction

Pancreatic cancer remains one of the deadliest malignancies worldwide, characterized by high mortality and poor prognosis, largely due to late-stage diagnosis [1]. Although long-term survival is possible with early detection of lesions with malignant potential, most patients with pancreatic cancer present irrecoverable stages [2]. Pancreatic cystic lesions (PCLs), particularly intraductal papillary mucinous neoplasms (IPMNs), represent a vital opportunity for early intervention, as they constitute identifiable precursors from which 15-20% of pancreatic cancers arise [3]. The clinical significance of these lesions has grown with improvements in cross-sectional imaging, longer lifespans, and increasing risk factors, with IPMN incidence now estimated at up to 49.1% on magnetic resonance imaging (MRI) [4]. These statistics underscore the critical need for improved methods of risk stratification for PCLs, particularly IPMN, which have a significant rate of progression to pancreatic cancer [5, 6].

PCLs have an estimated prevalence ranging from 4% to 14%, with autopsy studies demonstrating a prevalence as high as 50% in older populations [7]. The primary concern associated with PCLs is their potential for malignancy, as they are among the

few identifiable precursors to pancreatic ductal adenocarcinoma (PDAC) [4, 7]. The management of pancreatic cysts is determined by their risk of malignancy, which is classified as likely benign, low risk for malignancy, or potentially containing high-grade dysplasia or invasive carcinoma. The majority of pancreatic cysts are pseudocysts, serous cystic neoplasms (SCNs), mucinous cystic neoplasms (MCNs), or IPMNs [7]. While pancreatic pseudocysts and SCNs are benign, MCNs and IPMNs pose a risk of developing pancreatic cancer [7, 8]. Other types of PCLs, such as solid pseudopapillary neoplasms and cystic pancreatic neuroendocrine tumors, usually require surgical resection. However, these lesions are rare and generally less aggressive than MCNs and IPMNs with high-grade dysplasia or invasive carcinoma [7, 8]. Accurately identifying pancreatic cysts that could lead to cancer is crucial for early intervention. Additionally, there is a need for reliable and practical assessment methods for pancreatic cysts to minimize the risks of disease progression and complications from surgery.

Current clinical guidelines often struggle to accurately differentiate between high-risk and low-risk cysts [4, 9, 10]. This diagnostic uncertainty results in two concerning clinical scenarios: unnecessary surgical interventions with associated morbidity in patients with benign lesions, and missed opportunities for potentially curative intervention in patients with high-grade dysplasia or early invasive carcinoma [11–14]. The clinical paradox is evident in recent meta-analyses showing that 65–75% of resected IPMNs harbor only low-grade dysplasia, suggesting significant overtreatment, while other studies reveal cases of malignant transformation in lesions previously classified as low-risk [6, 9].

The primary non-invasive imaging techniques for evaluating pancreatic cysts are computed tomography (CT) and MRI/magnetic resonance cholangiopancreatography (MRCP) [7, 8, 15]. Most pancreatic cysts are initially identified through CT scans, but MRI/MRCP are preferred modalities for characterizing cysts and elucidating their relationship with the pancreatic ducts [4, 15, 16]. MRI/MRCP offers several advantages over CT, including better sensitivity for detecting duct communications, mural nodules, multiple cysts, and iso-attenuating PDAC [4]. According to the European Study Group guidelines, accuracy for identifying the specific type of PCLs is between 40% and 81% for CT and 40% and 95% for MRI/MRCP [16]. Additionally, MRI does not expose patients to ionizing radiation, making it especially valuable for individuals requiring frequent imaging as part of long-term surveillance [4, 7, 8]. However, unique challenges associated with interpreting MRI of the pancreas include inter-observer differences in experience, lack of standardization across different scanners, and significant variation in pancreatic shape and size among patients. To address these challenges, machine learning—particularly deep learning—can potentially enhance the diagnostic sensitivity and accuracy of MRI and MRCP in assessing and characterizing pancreatic cystic lesions. Despite recent advances, public datasets for pancreatic imaging remain scarce and are predominantly CT-based (*e.g.*, NIH Pancreas-CT [17]), constraining the development and validation of MRI-specific AI models. This scarcity underscores the novelty and importance of the *Cyst-X* dataset, which offers the first large-scale, multi-institutional MRI resource for pancreatic cystic lesion analysis. In addition, to overcome real-world barriers such as data silos and privacy laws like HIPAA [18]

and GDPR [19], we hypothesize that federated learning enables collaborative model training without sharing patient data.

Artificial intelligence (AI), particularly deep learning, has emerged as a powerful tool to improve diagnostic precision in medical imaging. While recent advances have demonstrated success across a range of radiological tasks, pancreatic imaging remains uniquely challenging due to the subtle presentation of early malignant changes and the limited availability of large, annotated datasets. These challenges are further compounded by privacy regulations and data governance policies that restrict the sharing of multi-institutional data, thereby impeding the development of robust, generalizable AI models for pancreatic disease diagnosis.

In this context, prior research on pancreas segmentation and IPMN classification has laid an important foundation. Pancreas segmentation research has predominantly focused on CT imaging, with limited exploration of MRI due to data scarcity [20]. Cai *et al.* proposed a recurrent neural network-based approach for pancreas segmentation, achieving a dice coefficient of 76.1% on 79 in-house T1-weighted (T1W) MRI scans [21]. Salanitri *et al.* introduced a multi-headed decoder structure that generates intermediate segmentation maps and ensembles these predictions to produce the final output. Their method achieved a dice coefficient of 77.5% on 40 in-house T2-weighted (T2W) MRI scans [22]. To date, Zhang *et al.* developed the largest pancreas segmentation dataset, comprising 767 MRI scans (385 T1W and 382 T2W) from 499 participants, and the PanSegNet model achieved dice coefficients of 85.0% for T1W MRI and 86.3% for T2W MRI [23]. Despite these advances, pancreas segmentation from MRI remains an underexplored area, with significant opportunities for further research and development.

For IPMN classification, early radiomics-based approaches by Chakraborty *et al.* [24] and Cui *et al.* [25] reported AUCs up to 0.88 using features extracted from manually segmented cysts, with a predominant focus on branch-duct IPMNs. However, main-duct IPMNs, which have a significantly higher risk of malignancy [4, 5, 10], remain relatively underrepresented. Deep learning methods have evolved from 2D CNN-based feature extractors [26] to fully end-to-end 3D models such as DenseINN and InceptINN [27], which adapt pre-trained 2D weights through an “inflation” mechanism. Corral *et al.* developed a CNN-based deep learning protocol to classify IPMN malignancy from MRI in a cohort of 139 cases and reported an AUC of 0.78, comparable to the Fukuoka (0.77) and American Gastroenterology Association (0.76) guidelines [5]. Transformer-based models [28] and hybrid frameworks that combine segmentation, radiomics, and deep learning predictions [29] have also demonstrated improved classification performance. Despite these advances, pancreas MRI segmentation and IPMN classification remain active research areas, with an urgent need for large-scale, multi-institutional datasets and integrative models capable of leveraging both anatomical and textural features for robust malignancy risk prediction.

To address these challenges, we collected 1,461 MRI scans (723 T1W and 738 T2W) from 764 unique patients across seven clinic centers: New York University Langone Health (NYU), Mayo Clinic Florida (MCF), Northwestern University (NU), Allegheny Health Network (AHN), Mayo Clinic Arizona (MCA), Istanbul University Faculty of Medicine (IU), and Erasmus Medical Center (EMC). Then, we hypothesized

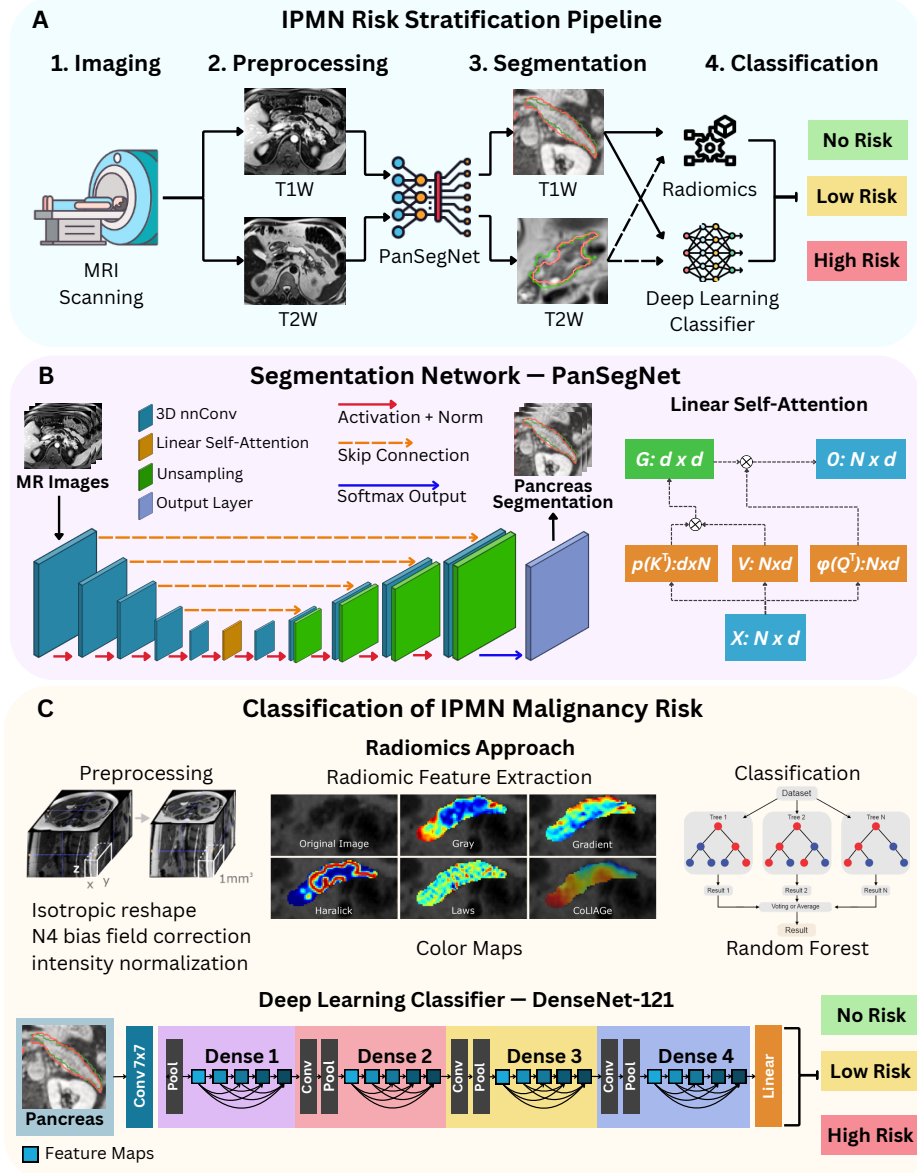


Fig. 1: Cyst-X Pipeline. (A) T1W and T2W MRI scans were collected from seven medical centers. (B) PanSegNet segments the pancreas: MRI scans are input into a pre-trained PanSegNet model to extract pancreas regions. To reduce computational cost, linear self-attention is used at the bottleneck (highlighted in yellow) instead of standard self-attention. (C) Radiomics analysis and deep learning classification assess the malignancy risk of IPMNs: In the radiomics pipeline, scans undergo resizing, bias field correction, and intensity normalization, followed by textural features extraction and a random forest classification model. In the deep learning pipeline, DenseNet-121 serves as the backbone for malignancy risk prediction.

that advanced deep learning models trained on diverse MRI data could significantly enhance IPMN risk stratification, outperforming current clinical guidelines and expert radiologist assessments. We further posited that federated learning could maintain comparable performance while preserving patient privacy and enabling cross-institutional collaboration. In summary, we present *Cyst-X* (illustrated in Figure 1), a comprehensive framework for pancreatic cyst analysis and risk stratification that makes the following contributions:

1. **Large-scale multi-center dataset:** *Cyst-X* includes 723 T1W and 738 T2W MRI images with radiologist-annotated ground truth segmentations collected from seven clinic centers. The dataset predominantly contains images of IPMNs (90-95%) and provides a significant resource for domain generalization studies, benchmarking new methods, and addressing other abdominal imaging tasks. Unlike existing CT-based datasets, *Cyst-X* fills a critical gap by offering MRI-based data, enabling standardized studies across diverse populations and institutions. Its combination of scale, diversity, and multi-modality makes it well-suited for developing and evaluating robust AI models in pancreatic cyst analysis and beyond.
2. **Advanced segmentation and classification:** We integrate PanSegNet, a state-of-the-art pancreas segmentation network, with innovative deep learning classification approaches that significantly outperform current clinical guidelines in identifying high-risk lesions. Our approach integrates radiomics with deep learning, enabling the extraction and analysis of subtle imaging features associated with malignant transformation. We also establish benchmarks for pancreas segmentation and IPMN risk classification using *Cyst-X*. For segmentation, we evaluate SwinUNETR [30] and PanSegNet [23]. For IPMN pancreatic cancer risk prediction, we apply radiomics-based and deep-learning-based methods such as DenseNet-121 [31] on both T1W and T2W MRI scans.
3. **Privacy-preserving federated learning:** We demonstrate the feasibility of training effective models across institutions without sharing sensitive patient data, addressing a critical barrier to clinical AI implementation.
4. **Public resource creation:** We release the *Cyst-X* dataset, segmentation algorithms, and classification models to accelerate research and development in pancreatic cancer early detection.

This work represents a significant advancement in pancreatic cancer risk stratification, with potential implications for clinical practice, patient outcomes, and the broader application of AI in medical imaging. Our study was approved with IRB number: STU00214545 by Northwestern University. We implemented a Data User Agreement with other centers. Our IRB approval serves as a primary record, and other institutions provide our IRB protocol within their local IRBs. Our IRB waived the informed consent of the study participants. The images were de-identified at their centers and transferred to our center fully anonymized (*i.e.*, the patient-protected health information was removed from the DICOM files before their transfer).

2 Results

2.1 UMAPs of quality indicators on T1W and T2W modalities

UMAP (Uniform Manifold Approximation and Projection) is a technique that reduces high-dimensional data to two or three dimensions for easier visualization. We employed UMAP to analyze image quality differences across centers and assess how scanning parameters vary. Figure 2 shows the UMAPs of quality indicators on T1W and T2W modalities, respectively, plotting with different colors in each center or each range of z thickness. In the T1W projections, some clusters are composed of centers with similar z-thickness. One mixed cluster consists of the NWU and IU centers (green and brown, respectively), both of which have a mean z-thickness of 3.3 mm. Other isolated clusters are composed of EMC (pink), MCF (orange), and NYU (blue) centers, with mean z-thicknesses of 2.5 mm, 4.9 mm, and 5.3 mm, respectively. Similarly, in the T2W projections, one mixed cluster consists of the NWU and NYU centers (green and blue), with mean z-thicknesses of 5.6 mm and 5.3 mm, respectively. Other isolated clusters are composed of the EMC (pink) and MCF (orange) centers, with mean z-thicknesses of 6.8 mm and 4.9 mm, respectively. These results show the quality differences across centers and the direct impact of z-thickness on the resolution.

Table 1: Benchmarking for Segmentation of Pancreas from MRIs.

Method	Dice(%)	Jaccard(%)	Precision(%)	Recall(%)	HD95(mm)	ASSD(mm)
T1W Modality						
PanSegNet	86.81±7.30	77.32±9.74	86.56±8.59	87.84±7.80	5.81±10.90	1.30±1.55
Swin-UNETR	79.09±1.40	67.19±1.63	79.09±1.67	81.37±0.74	26.55±8.48	7.58±3.76
+FedAvg	71.26±2.59	58.30±2.74	69.74±3.09	77.13±1.34	43.65±8.60	14.77±5.01
+FedProx($\mu=0.3$)	57.24±3.41	44.16±2.85	56.85±4.33	62.93±2.80	87.27±8.34	31.99±6.19
+FedProx($\mu=0.01$)	68.95±3.30	56.09±3.37	67.33±3.37	75.11±2.68	52.82±9.97	18.76±5.41
+FedProx($\mu=0.005$)	69.77±2.90	56.88±2.98	68.16±2.98	75.82±2.39	49.61±8.55	17.51±5.39
T2W Modality						
PanSegNet	89.62±6.38	81.73±9.31	90.74±6.45	89.11±8.06	4.19±4.99	0.75±0.87
Swin-UNETR	76.29±0.66	63.77±0.82	78.70±2.14	76.86±1.21	28.53±7.01	7.57±2.60
+FedAvg	69.19±1.51	55.48±1.44	70.52±2.98	71.31±0.95	41.87±5.84	11.74±3.02
+FedProx($\mu=0.3$)	58.11±2.61	43.85±2.22	59.01±4.38	61.46±1.11	66.68±9.10	20.87±4.81
+FedProx($\mu=0.01$)	67.25±1.86	53.47±1.77	68.22±2.99	70.23±1.21	48.36±6.51	14.52±3.64
+FedProx($\mu=0.005$)	67.82±1.44	54.16±1.43	68.63±2.41	70.89±0.84	48.64±5.82	13.99±2.96

2.2 Superior performance of PanSegNet for pancreas segmentation

Accurate pancreas segmentation is a critical prerequisite for precise cyst analysis and classification. Recently, we developed PanSegNet [23], a novel segmentation architecture incorporating linear self-attention layers [32] within the nnUNet framework [33]

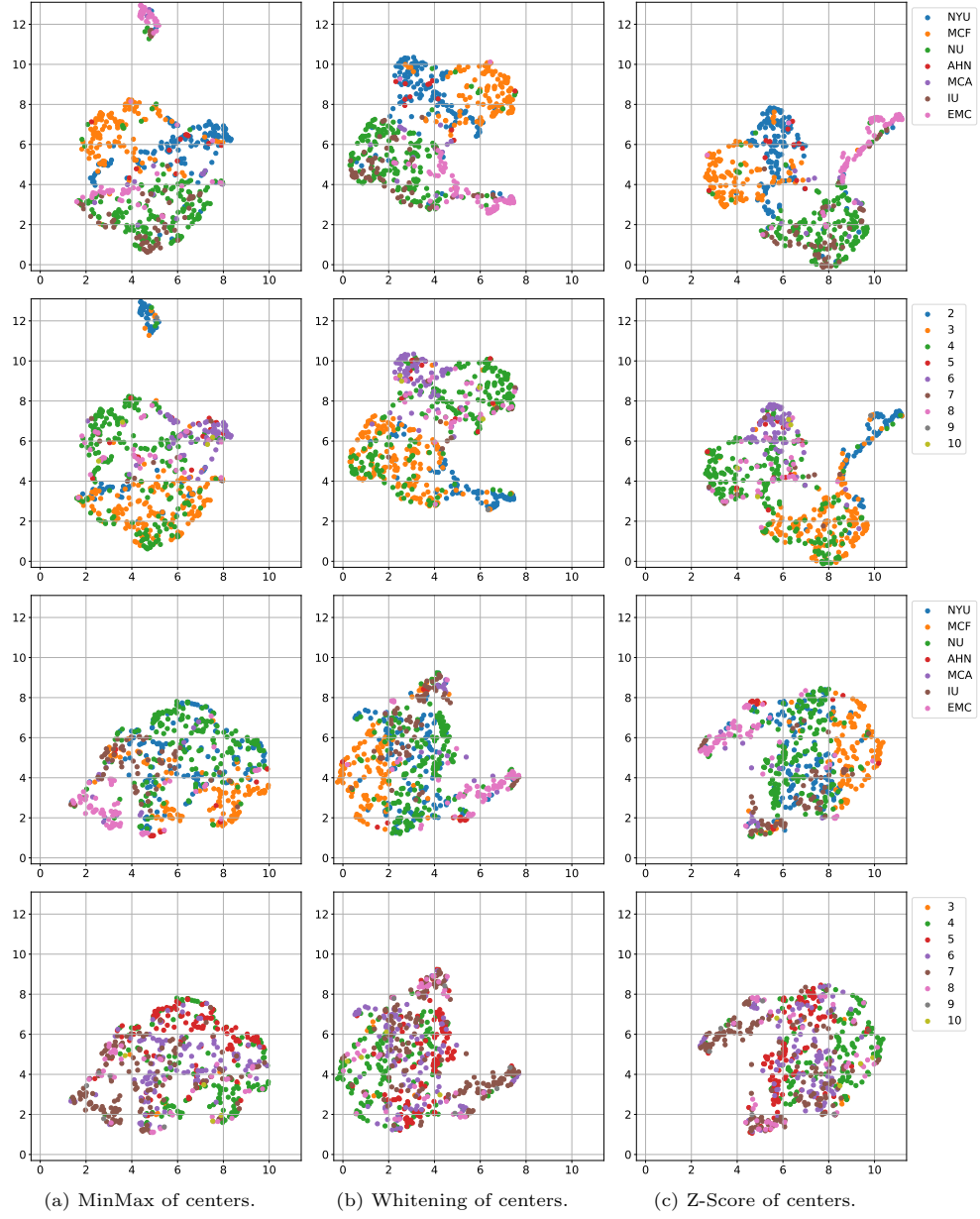


Fig. 2: MRQy analysis. Row 1: T1W modality MRQy of each center. Row 2: T1W modality MRQy of thickness range. Row 3: T2W modality MRQy of each center. Row 4: T2W modality MRQy of thickness range.

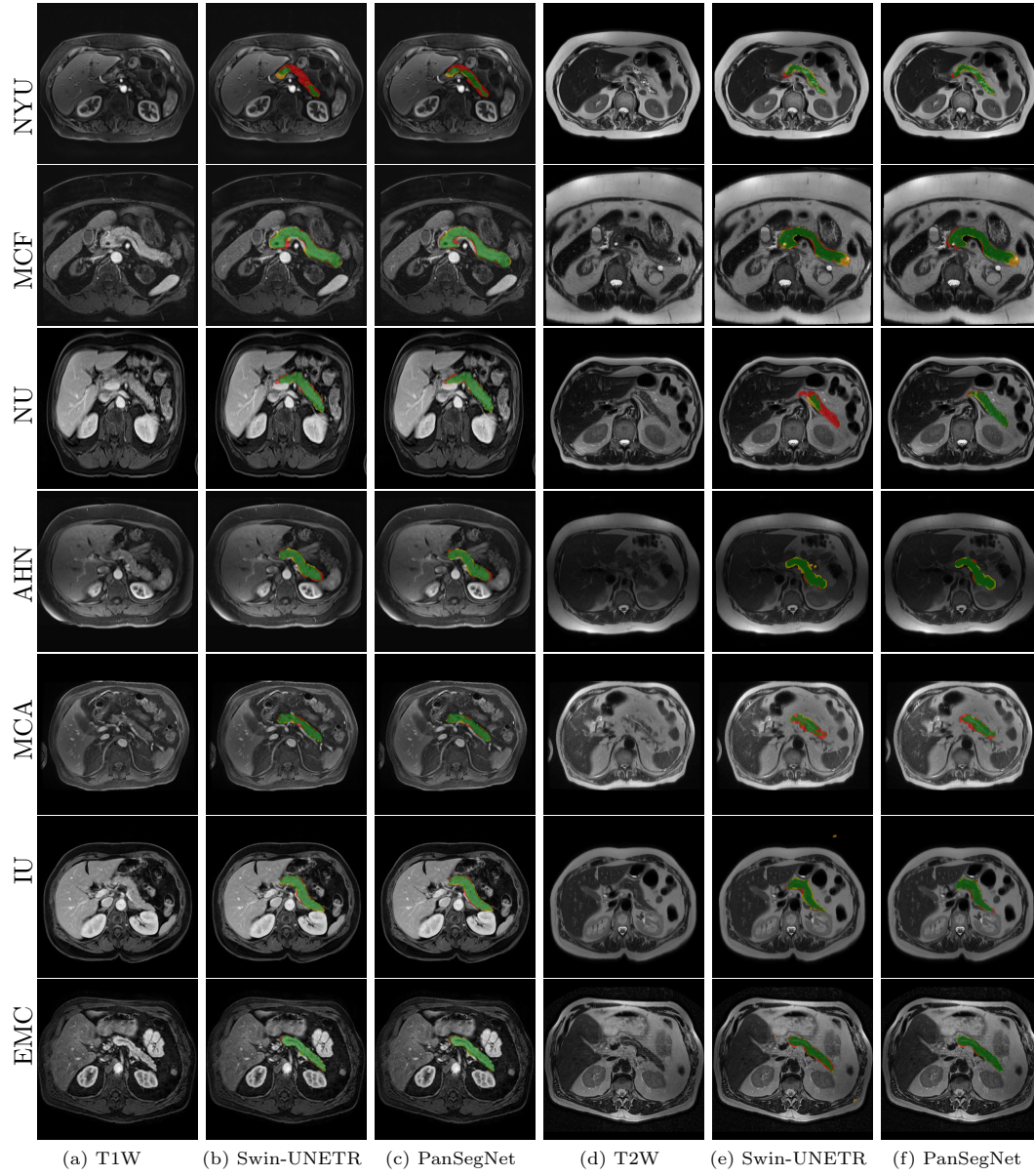


Fig. 3: *Cyst-X* Segmentation Results. Annotation masks are displayed in red. Model outputs are shown in green and yellow, with green indicating the overlap between the annotation masks and the model outputs.

to enhance global information modeling capabilities while maintaining computational efficiency (Fig. 1). PanSegNet demonstrated exceptional segmentation performance across both T1W and T2W modalities, achieving mean dice scores of $86.81 \pm 7.30\%$ and $89.62 \pm 6.38\%$, respectively (Table 1, Fig. 3b-c). This performance significantly exceeded that of Swin-UNETR [30], one of the most used state-of-the-art transformer-based medical segmentation models, which achieved dice scores of $79.09 \pm 1.40\%$ and $76.29 \pm 0.66\%$ for T1W and T2W, respectively ($p < 0.001$). In this study, we integrated PanSegNet into our *Cyst-X* engine along with a classifier for risk prediction. In Section 2.3, we show that the choice of segmentation model affects the classification results. The performance advantage of PanSegNet was consistent across all seven medical centers, demonstrating robust generalization despite variations in imaging protocols and equipment (Table 1). This cross-institutional reliability is particularly important for clinical applications, where model performance must remain consistent regardless of imaging site or acquisition parameters.

Table 2: IPMN Classification Results. Performance metrics for binary classification (high-risk vs. non-high-risk IPMN) and three-class classification (no-risk, low-risk, high-risk), with multiply-accumulate operations (MACs) and parameter counts provided to compare model computational efficiency and complexity.

Method	MACs Param.		T1W Modality		T2W Modality	
			ACC(%)	AUC(%)	ACC(%)	AUC(%)
Radiomics approach binary classification, four-fold cross-validation, multi-center dataset approach						
2D Radiomics features	-	-	68.76 ± 3.65	72.93 ± 3.23	71.57 ± 4.64	75.67 ± 6.24
3D Radiomics features	-	-	76.97 ± 3.90	77.98 ± 5.98	72.72 ± 3.91	75.75 ± 4.98
Deep learning three-class classification, five-fold cross-validation, pooled dataset approach						
ResNet-34	183.04G	63.47M	56.62 ± 9.13	72.01 ± 5.27	58.57 ± 3.81	78.63 ± 2.04
ShuffleNet-V2	0.57G	1.3M	46.65 ± 9.03	65.63 ± 3.80	58.49 ± 3.82	71.50 ± 3.08
MobileNet-V2	2.06G	2.36M	49.52 ± 5.30	65.49 ± 4.64	45.48 ± 7.88	65.76 ± 2.25
EfficientNet-B0	1.21G	4.69M	55.49 ± 2.75	68.07 ± 1.57	59.37 ± 5.78	74.41 ± 4.10
DenseNet-121	18.31G	11.25M	58.69 ± 4.28	75.59 ± 7.05	65.89 ± 4.98	81.09 ± 4.10
Federated learning binary classification, four-fold cross-validation, multi-center dataset approach						
DenseNet-121, centralized	18.31G	11.24M	79.90 ± 1.52	78.13 ± 2.06	78.23 ± 5.09	82.37 ± 1.02
DenseNet-121, FedAvg	18.31G	11.24M	79.29 ± 2.04	76.19 ± 1.02	81.08 ± 1.69	81.24 ± 2.98
DenseNet-121, FedProx($\mu = 0.1$)	18.31G	11.24M	78.52 ± 1.23	76.46 ± 1.21	78.29 ± 2.87	81.35 ± 1.77
DenseNet-121, FedProx($\mu = 0.3$)	18.31G	11.24M	75.26 ± 4.90	76.67 ± 1.09	79.27 ± 2.41	81.81 ± 2.15
Benchmarking Segmentation Network+DenseNet-121 for exploring the effect of segmentation model						
PanSegNet+3-class DenseNet-121	-	-	56.02 ± 8.23	72.26 ± 5.35	57.41 ± 1.26	74.18 ± 1.29
Swin-UNETR+3-class DenseNet-121	-	-	51.72 ± 8.75	66.95 ± 6.62	55.55 ± 2.74	69.63 ± 2.92
PanSegNet+2-class DenseNet-121	-	-	78.85 ± 3.16	74.84 ± 3.83	70.78 ± 10.48	77.01 ± 1.82
Swin-UNETR+2-class DenseNet-121	-	-	76.82 ± 2.44	70.20 ± 5.07	70.47 ± 11.47	68.92 ± 4.55

2.3 *Cyst-X* classification models outperform clinical guidelines and expert radiologists

We evaluated multiple approaches for IPMN risk classification, comparing radiomics-based methods with deep learning models, and benchmarking against both established clinical guidelines and expert radiologist assessments. Our 3D DenseNet-121 model achieved superior performance in distinguishing high-risk from low-risk and no-risk IPMNs (Table 2). In a direct comparison with the Kyoto Criteria [4], our model demonstrated significantly improved diagnostic accuracy ($\text{AUC}=82.37\pm1.02\%$ vs. $\text{AUC}\sim75\%$, $p < 0.01$) for T2W images. Notably, the performance improvement was most substantial in detecting high-risk lesions (sensitivity 87.8% vs. 64.1%, $p < 0.001$), which is clinically critical for preventing missed opportunities for early intervention. To further interpret the model’s feature representation, we performed t-SNE visualization of both the input images and the hidden states from the DenseNet-121. As shown in Fig. 4, input features show limited separation across risk classes, while the learned embeddings exhibit improved clustering by risk category. This indicates that the model successfully learns discriminative representations for IPMN risk stratification.

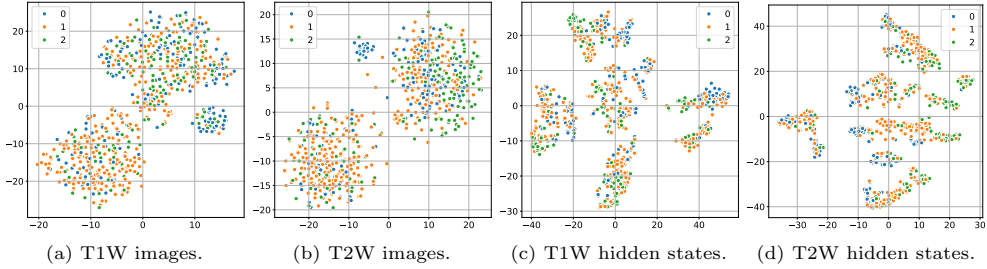


Fig. 4: t-SNE Visualization. 0: No risk. 1: Low risk. 2: High risk.

Among the classification approaches evaluated, the 3D radiomics features consistently outperformed 2D features ($\text{AUC}=78.26\pm4.28\%$ vs. $72.93\pm3.23\%$, $p < 0.05$), highlighting the importance of volumetric analysis for capturing the complex spatial characteristics of pancreatic lesions. The 3D DenseNet-121 further improved on radiomics-based methods ($\text{AUC } 82.37\pm1.02\%$ vs. $78.26\pm4.28\%$, $p < 0.01$), demonstrating the advantage of end-to-end deep learning for this task (Table 2).

To assess the importance of accurate pancreas segmentation in classification, we evaluated how different ROI sources affect DenseNet-121’s performance. Specifically, we compared classification results using ROIs generated by PanSegNet and Swin-UNETR, both under centralized learning, against a baseline using radiologist-defined ROIs. As shown in Table 2, using PanSegNet’s masks resulted in only a modest performance decline, reflecting its strong segmentation quality. In contrast, Swin-UNETR led to a more substantial drop, demonstrating that inferior segmentation can directly compromise classification. For 3-class classification, the mean

Table 3: Comparison of IPMN Classification Accuracy: Radiologists vs. DenseNet-121. DenseNet-121 with probability fusion outperformed the average radiologists’ performance in both no/low-risk and high-risk classification accuracy.

Method	Input Modality	No/Low-Risk	High-Risk
Radiologist 1	T1W+T2W	89.94	64.08
Radiologist 2	T1W+T2W	97.13	32.39
Radiologist 3	T1W+T2W	94.66	41.55
Average	T1W+T2W	93.91	46.01
DenseNet-121	T1W Only	91.38	40.85
DenseNet-121	T2W Only	86.11	53.96
DenseNet-121(feature fusion)	T1W+T2W	95.69	43.66
DenseNet-121(probability fusion)	T1W+T2W	94.66	47.18

AUC dropped from 75.59% (radiologist ROI) to 72.26% with PanSegNet, and further to 66.95% with Swin-UNETR on T1-weighted images. On T2-weighted scans, the AUC declined from 81.09% to 74.18% (PanSegNet) and to 69.63% (Swin-UNETR). A similar trend was observed in 2-class classification: on T1W, AUC dropped from 78.13% to 74.84% (PanSegNet) and 70.20% (Swin-UNETR); on T2W, from 82.37% to 77.01% and 68.92%, respectively. These results emphasize that accurate segmentation—particularly via PanSegNet—is not only essential for volume estimation but also critical to preserving downstream classification performance in the *Cyst-X* pipeline.

Furthermore, when compared with the visual assessments of three expert radiologists ($n = 3$), our models demonstrated superior accuracy in both no/low-risk and high-risk cases. As shown in Table 3, the DenseNet-121 model with probability fusion achieved a no/low-risk classification accuracy of 94.66% and a high-risk accuracy of 47.18%, outperforming the radiologists’ average accuracies of 93.91% and 46.01%, respectively. While this overall performance suggests that *Cyst-X* surpasses expert-level assessments, a more nuanced interpretation is warranted. Notably, Radiologist 2 achieved the highest no/low-risk classification accuracy at 97.13%, exceeding that of any model configuration. However, their high-risk accuracy was substantially lower at just 32.39%. This indicates a conservative diagnostic tendency, which is likely prioritizing avoidance of false positives at the expense of missing high-risk cases. In contrast, our model maintained a more balanced performance across risk categories, demonstrating both strong sensitivity and specificity. This balance suggests that *Cyst-X* is not only more accurate overall but also potentially more reliable in clinical decision-making, where both under- and over-diagnosis carry significant consequences. For visual explainability of classification results, visual saliency-based methods are often used, although most of such methods are not true explanation methods, but show mostly learned patterns in the image region in correlation to the result. For this purpose, GradCAM [34] and Information Bottleneck Attribution (IBA) [35, 36] based visualizations were generated (See Supplementary materials).

2.4 Privacy-preserving federated learning maintains high performance

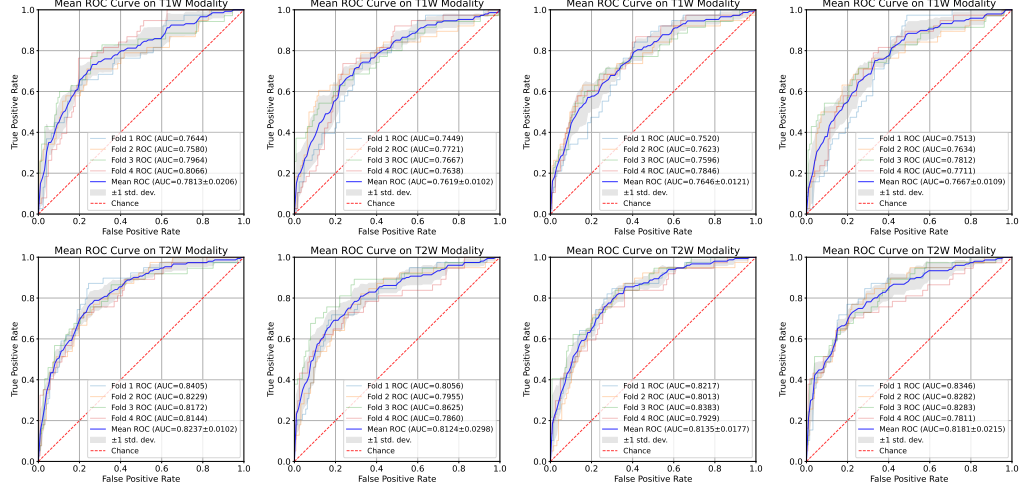
To address privacy concerns that often restrict data sharing across institutions, we implemented and evaluated federated learning approaches for both segmentation and classification tasks. Using Federated Averaging (FedAvg) [37] and Federated Proximal (FedProx) [38] algorithms, we trained models across distributed datasets without sharing patient data. For the segmentation task, federated learning approaches showed reduced performance compared to centralized training, with dice score decreases of 7.83% and 7.10% for T1W and T2W modalities, respectively, using FedAvg (Table 1). This performance gap likely stems from the high sensitivity of segmentation tasks to data heterogeneity across institutions.

In contrast, our classification models maintained robust performance in the federated setting. FedProx with $\mu = 0.3$ achieved the best average AUCs (76.67% on T1W and 81.81% on T2W modalities) among all federated learning configurations. Its results were close to the centralized baseline, with only 1.46% and 0.56% decrease on T1W and T2W modalities, respectively. FedProx with $\mu = 0.1$ also outperformed FedAvg, yielding AUCs of 76.46% on T1W and 81.35% on T2W, compared to FedAvg’s 76.19% and 81.24%. Since FedAvg can be treated as a special FedProx case with $\mu = 0$, these findings indicate that moderately strong proximal regularization stabilizes training and enhances performance in heterogeneous multi-institutional settings for the IPMN classification task. These findings are further illustrated in Fig. 5, which shows the ROC curves for each method across both T1W and T2W modalities. Each subfigure presents the mean ROC curve over four cross-validation folds, along with individual fold performance and standard deviation bands. The centralized model consistently achieved the highest AUCs, serving as an upper-bound benchmark. Among federated methods, FedProx with $\mu = 0.3$ produced the most favorable results, with ROC curves closely aligned with the centralized baseline. Compared to FedAvg, both FedProx configurations achieved higher mean AUCs and demonstrated reduced variability across folds, particularly on the T2W modality. These visual results corroborate our findings, demonstrating that moderately strong proximal regularization improves model generalization and stability in federated learning for multi-center IPMN classification.

This preservation of classification performance in the federated setting is particularly significant, as it enables multi-institutional collaboration while maintaining regulatory compliance, a critical consideration for clinical deployment of AI tools.

3 Discussion

Our study presents *Cyst-X*, a comprehensive AI framework for pancreatic cyst analysis and risk stratification that demonstrates superior performance compared to current clinical guidelines and expert radiologists. By leveraging deep learning on a large, multi-center MRI dataset, we have developed models capable of identifying subtle imaging features associated with malignant transformation, potentially enabling earlier intervention for high-risk lesions and reducing unnecessary procedures for benign cysts.



(a) Centralized Learning. (b) FedAvg [37]. (c) FedProx ($\mu = 0.1$) [38]. (d) FedProx ($\mu = 0.3$) [38].
Fig. 5: ROC curves for Multi-Center IPMN MRI binary classification Using DenseNet-121.

The performance improvement over established clinical guidelines (AUC=0.82 vs. AUC=0.75) represents a clinically meaningful advance that could significantly impact patient management. The higher sensitivity for detecting high-risk IPMNs suggests potential for identifying cases that might be missed by conventional assessment, while improved specificity could reduce unnecessary surgical interventions and their associated morbidity. This balance is particularly crucial in pancreatic cyst management, where both under-treatment and over-treatment carry significant consequences.

Perhaps equally important is our demonstration that these models can be effectively trained in a federated learning environment without compromising performance. This approach addresses critical barriers to clinical AI implementation, enabling institutions to collaborate while maintaining regulatory compliance and preserving patient privacy. The slight performance reduction observed in federated versus centralized learning (AUC decrease of approximately 0.01-0.02) represents a reasonable trade-off for these substantial privacy benefits.

The integration of advanced segmentation through PanSegNet with classification models represents a comprehensive approach to pancreatic imaging analysis. By first accurately delineating the pancreas, which is a notoriously challenging organ to segment, our system creates a foundation for more precise feature extraction and classification. The superior performance of 3D compared to 2D radiomics features further emphasizes the importance of comprehensive volumetric analysis in capturing the complex spatial characteristics of pancreatic lesions.

While PanSegNet achieved high segmentation accuracy overall, its performance was modestly lower in the federated learning setting compared to centralized training. This performance gap highlights a well-known challenge in federated learning for

segmentation tasks, particularly under high data heterogeneity across institutions. To address this, future work could explore advanced aggregation methods such as Federated Matched Averaging (FedMA) [39], which aligns intermediate representations prior to model fusion, thereby reducing inter-site domain discrepancies. Additionally, techniques from federated domain adaptation [40, 41], federated domain generalization [42–45], and cycle-consistency constraints [46] may further enhance robustness to distributional shifts. These strategies offer promising avenues to close the segmentation performance gap in federated learning settings while maintaining privacy, ultimately making federated learning more viable for complex, multi-institutional medical imaging tasks. Moreover, in *Cyst-X*, we designed our federated learning implementation to keep patient data decentralized, ensuring that raw MRI scans never leave their originating institutions. However, we did not integrate formal privacy-preserving mechanisms such as differential privacy or secure aggregation. As we move toward real-world deployment and tighter regulatory landscapes, future work should focus on incorporating these techniques to provide stronger, provable guarantees of patient privacy. For instance, differentially private federated averaging (DP-FedAvg) [47, 48] introduces noise to model updates to ensure individual data contributions remain indistinguishable, while secure aggregation protocols [49] allow encrypted model updates to be aggregated without revealing individual contributions.

Our observation that certain AI-identified imaging features correlate strongly with known markers of malignancy suggests the potential for these models to identify novel biomarkers or enhance our understanding of existing ones. This aspect merits further investigation, as it may reveal imaging characteristics that are not readily apparent to human observers but hold diagnostic significance.

While our findings demonstrate promise, several limitations warrant discussion. The retrospective nature of our study, though partially offset by sample size and institutional diversity, introduces potential selection biases. The evolution of MRI technology and protocols over our collection period (2004-2024) may introduce temporal variations in image quality and characteristics. Additionally, while our dataset is diverse in terms of institutional sources, further validation across different demographic populations would strengthen generalizability claims.

Integrating *Cyst-X* into clinical practice will assist clinicians in the management of cystic pancreatic lesions in several aspects. Given the high prevalence of pancreatic cysts and the risk of missing small ones, it will serve as both a guide for detection and a decision support tool for cyst classification. More importantly, due to the complexity of pancreatic cyst management, it can directly influence patient management, such as follow-up or intervention, in more complex cases that cannot be clearly classified radiologically or clinically according to current international guidelines. However, implementing it in practice will require prospective validation studies to ensure that it performs effectively in real-world settings and user interface development to incorporate these tools into radiological workflows seamlessly. In addition, clinical trials with well-defined patient groups will further validate and improve the algorithm’s performance. Future research should also focus on combining imaging features with clinical and molecular data to improve risk stratification.

In conclusion, *Cyst-X* represents a significant advancement in pancreatic cancer risk assessment, demonstrating the potential of AI to improve early detection of malignant transformation in pancreatic cystic lesions. By making our dataset, algorithms, and models publicly available, our objective is to accelerate research in this field and foster collaborative development that could ultimately improve outcomes for patients with this devastating disease.

4 Methods

4.1 Construction and characteristics of the Cyst-X dataset

The *Cyst-X* dataset involves 1,461 MRI scans (723 T1W and 738 T2W) from 764 unique patients. These patients were 18 or older, collected between March 2004 and June 2024 across seven international medical centers: New York University (NYU) Langone Health, Mayo Clinic Florida (MCF), Northwestern University (NU), Allegheny Health Network (AHN), Mayo Clinic Arizona (MCA), Istanbul University Faculty of Medicine (IU), and Erasmus Medical Center (EMC). Dataset composition is summarized in Table 4. The MRI scans were obtained from diverse imaging devices, including GE, Siemens, and Philips. The diversity of data sources enhances the robustness and generalizability of our deep learning models, reflecting the real-world clinical variations and scenarios. Each scan includes the corresponding ground truth pancreas segmentation and malignancy risk classification. Patient demographics were well-balanced across centers, with mean ages ranging from 50.9 to 71.1 years and appropriate gender distribution. To ensure consistency across institutions, we developed a rigorous inclusion protocol based on histopathological confirmation or extended imaging follow-up, which defined three categories for classification:

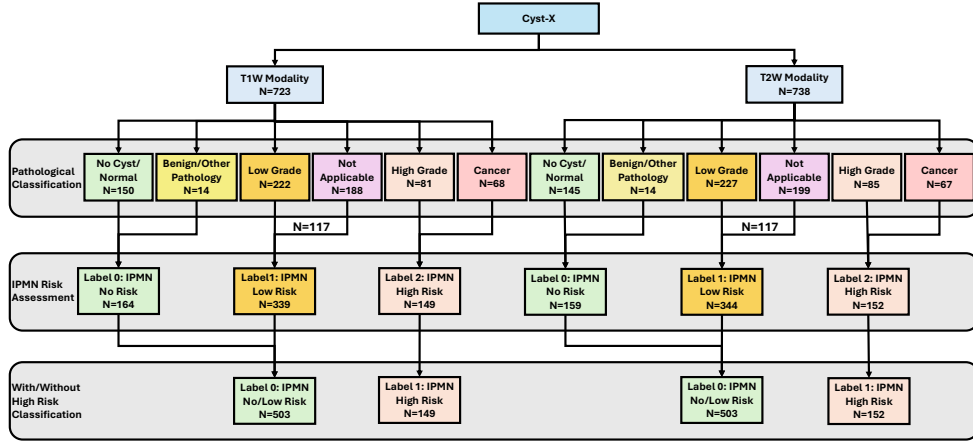
1. **High-risk:** IPMN cases with high-grade dysplasia or worse (including carcinoma in situ and invasive cancer), confirmed by EUS-guided biopsy or surgery. Only MRI scans obtained within six months of the confirmatory procedure were included.
2. **Low-risk:** IPMN cases with low- or intermediate-grade dysplasia confirmed histologically, or presumed low-risk IPMNs without biopsy that showed no progression over at least three years of follow-up. No progression was defined as < 2.5 mm growth and absence of worrisome features or high-risk stigmata.
3. **No risk / Control:** Individuals with normal pancreatic imaging, no cystic lesions, or benign cysts not associated with IPMN.

Each patient was categorized into one of these three ground truth classes: no risk/control, IPMN low-risk, or IPMN high-risk. To evaluate variability in image acquisition, we applied uniform manifold approximation and projection (UMAP) to image quality indicators, revealing distinct clustering patterns by imaging center and slice thickness. This heterogeneity reflects real-world clinical variability, enhancing the dataset’s generalizability while presenting technical challenges for model development. Fig. 6 shows examples of low-grade, high-grade, and cancer developing IPMNs from the *Cyst-X* dataset.

In this study, diverse imaging devices and varying acquisition protocols were used to collect data. To evaluate the properties of the images, quality indicators are assessed,

Table 4: *Cyst-X* dataset composition. Data distribution is shown hierarchically below.

Data Centers	NYU	MCF	NU	AHN	MCA	IU	EMC
Imaging Device	Siemens, GE	Siemens, GE	Siemens	N/A	Siemens, GE	Siemens, Philips	Siemens, GE
MRI Magnet(T)	1.5, 3	1.5, 3	1.5, 3	N/A	1.5, 3	1.5, 1.5	1.5, 1.5
Demographics data for T1W modalities							
Patient Count	162	148	206	17	25	74	91
Female	98	81	109	12	14	42	43
Male	64	67	97	5	11	32	48
Mean Age(y)	63.0	65.0	63.9	N/A	71.1	64.1	50.9
Demographics data for T2W modalities							
Patient Count	162	143	207	27	23	73	103
Female	97	78	109	19	10	41	50
Male	65	65	98	8	13	32	53
Mean Age(y)	62.9	65.4	63.9	N/A	70.1	63.8	52.2



including statistical measures of intensity (*e.g.*, mean, range, variance) and second-order statistics or filter-based metrics (*e.g.*, contrast per pixel, entropy focus criterion, and signal-to-noise ratios). A total of 21 quality indicators were extracted using the open-source MRQy tool [50]. To calculate the uniform manifold approximation and projection (UMAP) for dimension reduction, each feature was normalized across the dataset using the following techniques:

- MinMax normalization:

$$x'_{minmax} = \frac{x - x_{min}}{x_{max} - x_{min}}, \quad (1)$$

- Whitening normalization:

$$x'_{whiten} = \frac{x}{\sigma}, \quad (2)$$

- Z-score normalization:

$$x'_{zscore} = \frac{x - \mu}{\sigma}, \quad (3)$$

where x and x' are the original and normalized values, respectively, while μ and σ are the mean and standard deviation of the dataset.

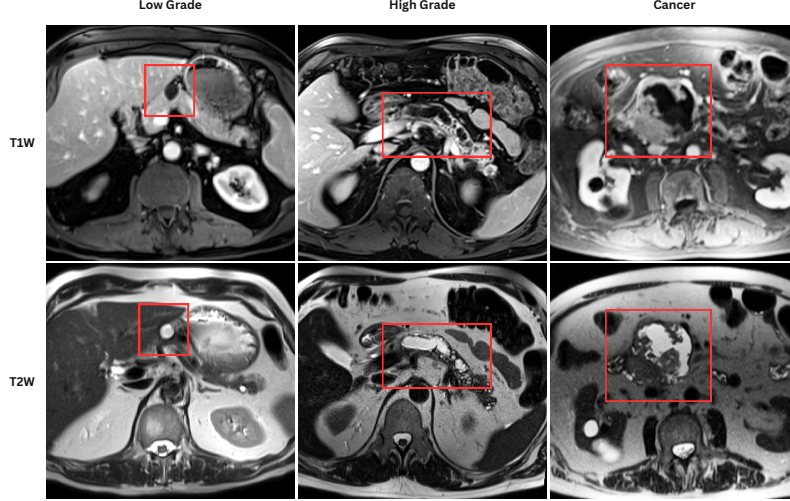


Fig. 6: Low grade, high grade, and cancer developing IPMNs from the *Cyst-X* dataset.

4.2 Image preprocessing and segmentation

All MRI scans were converted from DICOM to NIFTI format for processing. Then, expert radiologists manually segmented the pancreas to establish ground-truth annotations. The segmentation protocol was standardized between centers using ITK-SNAP software [51], and a senior radiologist reviewed all masks to ensure quality and consistency.

In this work, we adopted PanSegNet [23] for MRI pancreas segmentation, as shown in Figure 1. By incorporating the linear self-attention structure [52] into the nnUNet framework [33], PanSegNet enhances global information modeling capabilities while maintaining linear computational efficiency [32]. Formally, let $\mathbf{X} \in \mathbb{R}^{N \times d}$ denote the input feature matrix, where each row corresponds to an individual feature vector. Let $\mathbf{A}, \mathbf{A}' \in \mathbb{R}^{N \times N}$ represent the attention matrices computed by traditional and linear self-attention mechanisms, respectively. Here, N and d represent the length and the dimension of the feature, with $N > d$. The queries, keys, values $\mathbf{V}, \mathbf{Q}, \mathbf{K}, \in \mathbb{R}^{N \times d}$ are computed by linearly projecting the input features \mathbf{X} :

$$\mathbf{Q} = \mathbf{X}\mathbf{W}_Q + \mathbf{b}_Q, \quad (4)$$

$$\mathbf{K} = \mathbf{X}\mathbf{W}_K + \mathbf{b}_K, \quad (5)$$

$$\mathbf{V} = \mathbf{X}\mathbf{W}_V + \mathbf{b}_V, \quad (6)$$

where $\mathbf{W}_Q, \mathbf{W}_K, \mathbf{W}_V \in \mathbb{R}^{d \times d}$ and $\mathbf{b}_Q, \mathbf{b}_K, \mathbf{b}_V \in \mathbb{R}^d$ are learnable parameters.

The traditional self-attention is defined as:

$$\mathbf{A}_i = \sum_{j=0}^{N-1} \text{sim}(\mathbf{Q}_i, \mathbf{K}_j) \mathbf{V}_j, \quad (7)$$

where i, j index the input features, and the similarity function is defined as:

$$sim(\mathbf{q}, \mathbf{k}) = SoftMax \left(\frac{\mathbf{q}\mathbf{k}^T}{\sqrt{d}} \right). \quad (8)$$

In linear self-attention [52], the similarity function is approximated by decomposing it into two kernel feature maps:

$$sim'(\mathbf{q}, \mathbf{k}) = \phi(\mathbf{q})\rho(\mathbf{k})^T. \quad (9)$$

Here, $\phi(\cdot)$ and $\rho(\cdot)$ apply the SoftMax function to the queries row-wise and keys column-wise, respectively. The resulting linear self-attention is then computed as:

$$\mathbf{A}'_i = \sum_{j=0}^{N-1} \phi(\mathbf{Q}_i)\rho(\mathbf{K}_j)^T \mathbf{V}_j = \phi(\mathbf{Q}_i) \sum_{j=0}^{N-1} \rho(\mathbf{K}_j)^T \mathbf{V}_j, \quad (10)$$

This definition keeps the important property of original self-attention, *i.e.*, $\sum_{j=0}^{N-1} sim(\mathbf{Q}_i, \mathbf{K}_j) = 1$ and reduces the computational complexity from $O(dN^2)$ to $O(d^2N)$.

Training of PanSegNet followed the implementation described in [23]. We employed stochastic gradient descent (SGD) for optimization and adopted a systematic hyperparameter tuning strategy to balance efficiency and performance. Specifically, we set the learning rate to 0.01, used a batch size of 10, and trained the model for 600 epochs. To mitigate overfitting, we incorporated dropout layers and applied data augmentation techniques during training. However, since PanSegNet is based on nnUNet, implementing it within a federated learning framework is challenging due to its reliance on centralized dataset-specific configurations and the inherent heterogeneity of federated learning setups. nnU-Net dynamically adapts its architecture, preprocessing, and training hyperparameters based on global dataset statistics, which are inaccessible in federated learning due to privacy constraints and non-IID data distribution. Furthermore, nnUNet requires its specific training commands, which complicates integration with federated learning systems. To address this issue and for comparison, we also implemented Swin-UNETR [30]. It is a widely used MRI segmentation network, and is more suitable for federated learning as it can be easily implemented using pure PyTorch [53] and MONAI [54]. Both models were trained and evaluated using 5-fold cross-validation.

4.3 Radiologist Visual Scoring

Three independent expert radiologists visually evaluated the images according to the imaging features described in the Kyoto Criteria [4]. They had seven, four, and four years of experience in abdominal imaging, respectively, and they all had interpreted more than 2,000 abdominal MRIs, ensuring a high level of expertise in diagnosing and classifying complex abdominal conditions, including IPMN. The radiologists were unaware that most cysts had been confirmed as IPMNs, simulating real-life initial

assessments of cystic lesions. Additionally, the radiologists were blinded to the subjects’ clinical information, relied exclusively on contrast-enhanced T1W and T2W sequences, without access to previous imaging. In this study, 67 cases from the study cohort were excluded due to the lack of appropriate T1W or T2W images, and 68 patients were also excluded for not having ground truth risk assessment labels. As a result, a total of 629 cases were used for radiologist visual scoring. A pairwise assessment of accuracy and weighted kappa statistics was conducted to evaluate agreement among the raters. Furthermore, we assessed accuracy to determine how effectively the radiologists identified high-risk lesions.

4.4 Radiomics approach for IPMN classification

We extracted radiomic features that quantify the textural attributes of the entire pancreas. The preprocessing steps included reshaping, bias field correction, and intensity normalization. We conducted two separate analyses: one used the entire 3D pancreas volume to extract 763 features, while the other focused on 2D slices from the axial plane, extracting 447 features.

The extracted features encompassed spatial properties of pixel intensities to capture patterns such as edges, waves, spots, and ripples. These included categories like raw intensity, gray-level, gradient, and Laws’ texture energy features [55]. Additional features were derived from gray-level co-occurrence matrices (GLCM), such as Haralick features [56] and CoLIAGe features [57]. The Haralick features captured image heterogeneity, and the CoLIAGe features [57] identified localized gradient orientation changes. Multiple window sizes and numbers of bins were used to extract these features. Each feature was represented by four statistical metrics across the volume: median, standard deviation, skewness, and kurtosis.

At the end of this process, a total of 1,788 features were extracted for the 2D analysis and 3,052 features for the 3D analysis. Then, these features were selected via the maximum relevance minimum redundancy (mRMR) algorithm [58] and fed to a random forest model [59]. Finally, the random forest model determined whether the scans are IPMN high risk. The random forest model was trained with 50 iterations on the training split.

4.5 DenseNet-121 for IPMN Classification

In the deep learning approach, we utilized the 3D DenseNet-121 model [31] for the IPMN classification task. The ROIs in the MRI images were extracted and resized to dimensions of $96 \times 96 \times 96$ to serve as input to the models. For model training, we employed the AdamW optimizer [60] with an initial learning rate of 0.001 and a batch size of 16 over 100 epochs. The learning rate was progressively reduced by a factor of 10 every 30 epochs to enhance convergence. We implemented two versions of the DenseNet-121 model: one for three-class classification (no risk, low risk, or high risk) and another for binary classification (high risk vs. not high risk). For the three-class classification model, due to data sparsity, we used a pooled dataset approach and applied a stratified split across all images, disregarding their originating centers, to ensure a balanced representation of the categories. For the binary classification model,

we adopted a multi-center dataset approach and performed a stratified split separately within each center to account for potential inter-center variability in the data distribution. Performance was evaluated using 5-fold cross-validation for the three-class model and 4-fold cross-validation for the binary model.

We compared the performance of DenseNet-121 with several other prominent 3D deep neural networks, including ResNet-34 [61, 62], ShuffleNet-V2 [63], MobileNet-V2 [64], and EfficientNet-B0 [65], in the 3-class classification task. Each model was trained in two separate trials: one using T1W modality ROI images and the other using T2W modality ROI images.

We also compared the predictions generated by our DenseNet-121 model with the radiologists’ assessments. Model predictions were obtained using weights from cross-validation folds corresponding to each test case, and the resulting labels were aggregated for comparison with the radiologist assessments. To further enhance model performance and clinical applicability, we explored two fusion strategies to integrate T1W and T2W information: feature-level and probability-level fusion. In the feature-level fusion approach, features extracted from T1W and T2W images were concatenated after the backbone and passed through a shared classification layer. In the probability-level fusion approach, each modality was processed through separate classification heads, and the resulting probability outputs were combined via weighted averaging.

4.6 Federated learning implementation

To evaluate privacy-preserving distributed learning, we implemented both Swin-UNETR for segmentation and DenseNet-121 for classification within federated learning frameworks using FedAvg [37] and FedProx [38] algorithms. FedAvg aggregates model updates by averaging weights from participating clients. Formally, the update rule for the global model \mathbf{w}^t at epoch t is:

$$\mathbf{w}^t = \frac{\sum_{k=0}^{K-1} N_k \mathbf{w}_k^t}{\sum_{k=0}^{K-1} N_k}, \quad (11)$$

where, \mathbf{w}_k^t is the model update from the k -th client only using data belong to it, N_k is the number of samples from the k -th client, and K is the number of participating clients. In contrast, FedProx introduces a proximal term $\frac{\mu}{2} \|\mathbf{w}_k^{t+1} - \mathbf{w}^t\|^2$ to the loss function of each client ℓ_k to mitigate the impact of client drift and heterogeneous data, allowing for more stable convergence:

$$\ell_k^{\text{prox}}(t+1) = \ell_k(t+1) + \frac{\mu}{2} \|\mathbf{w}_k^{t+1} - \mathbf{w}^t\|^2, \quad (12)$$

For FedProx, we tested multiple values of the proximal term μ (0.3, 0.1, and 0.005) to identify optimal settings. Performance was compared with centralized training using the same evaluation metrics (dice scores for segmentation; accuracy and AUC for classification).

4.7 Statistical analysis and Visual attribute maps

Segmentation performance was evaluated using the dice coefficient, Jaccard index, precision, recall, 95th percentile Hausdorff distance (HD95), and average symmetric surface distance (ASSD). Classification performance was assessed through accuracy and area under the curve (AUC). Statistical significance was determined using paired t-tests or Wilcoxon signed-rank tests as appropriate, with $p < 0.05$ considered significant.

To interpret model predictions, we generated visual attribution maps using Grad-CAM [34] and IBA [35, 36]. Grad-CAM highlights spatial regions that strongly influence the model’s decision by computing gradients of the target class score with respect to feature activations. In contrast, IBA offers sharper and more focused explanations by learning a perturbation mask that minimizes mutual information between intermediate representations and predictions, thereby isolating only the most critical features for decision-making. Visualizations from both methods are provided in the Supplementary Materials.

5 Data Availability

The *Cyst-X* dataset, including anonymized MRI scans, segmentation masks, and risk labels, is publicly available at <https://osf.io/74vfs/>. The dataset is provided in NIFTI format with accompanying metadata.

6 Code Availability

Source code for the PanSegNet segmentation model and classification algorithms is available at <https://github.com/NUBagciLab/Cyst-X>.

7 Acknowledgments

This work was supported by NIH NCI R01-CA246704, R01-CA240639, U01-CA268808, NIH-NHLBI R01-HL171376, and NIH-NIDDK #U01 DK127384-02S1.

8 Author Contributions

H.P., Z.Z., conceived the study, performed data analysis, and drafted the manuscript. G.D., E.K., D.S., U.B. supervised the project, guided the experimental design, and critically revised the manuscript. All authors discussed the results and contributed to the final version of the manuscript.

9 Competing Interests

The authors declare no competing interest.

References

- [1] Stoffel, E.M., Brand, R.E., Goggins, M.: Pancreatic cancer: changing epidemiology and new approaches to risk assessment, early detection, and prevention. *Gastroenterology* **164**(5), 752–765 (2023)
- [2] Balaban, E.P., Mangu, P.B., Yee, N.S.: Locally advanced unresectable pancreatic cancer: American society of clinical oncology clinical practice guideline summary. *Journal of oncology practice* **13**(4), 265–269 (2016)
- [3] Tanaka, M., Fernández-del Castillo, C., Kamisawa, T., Jang, J.Y., Levy, P., Ohtsuka, T., Salvia, R., Shimizu, Y., Tada, M., Wolfgang, C.L.: Revisions of international consensus fukuoka guidelines for the management of ipmn of the pancreas. *Pancreatology* **17**(5), 738–753 (2017)
- [4] Ohtsuka, T., Fernandez-del Castillo, C., Furukawa, T., Hijioka, S., Jang, J.-Y., Lennon, A.M., Miyasaka, Y., Ohno, E., Salvia, R., Wolfgang, C.L., *et al.*: International evidence-based kyoto guidelines for the management of intraductal papillary mucinous neoplasm of the pancreas. *Pancreatology* **24**(2), 255–270 (2024)
- [5] Corral, J.E., Hussein, S., Kandel, P., Bolan, C.W., Bagci, U., Wallace, M.B.: Deep learning to classify intraductal papillary mucinous neoplasms using magnetic resonance imaging. *Pancreas* **48**(6), 805–810 (2019)
- [6] Yao, L., Zhang, Z., Keles, E., Yazici, C., Tirkes, T., Bagci, U.: A review of deep learning and radiomics approaches for pancreatic cancer diagnosis from medical imaging. *Current Opinion in Gastroenterology* **39**(5), 436–447 (2023)
- [7] Seyithanoglu, D., Durak, G., Keles, E., Medetalibeyoglu, A., Hong, Z., Zhang, Z., Taktak, Y.B., Cebeci, T., Tiwari, P., Velichko, Y.S., *et al.*: Advances for managing pancreatic cystic lesions: Integrating imaging and ai innovations. *Cancers* **16**(24), 4268 (2024)
- [8] Megibow, A.J., Baker, M.E., Morgan, D.E., Kamel, I.R., Sahani, D.V., Newman, E., Brugge, W.R., Berland, L.L., Pandharipande, P.V.: Management of incidental pancreatic cysts: a white paper of the acr incidental findings committee. *Journal of the American College of Radiology* **14**(7), 911–923 (2017)
- [9] Heckler, M., Michalski, C.W., Schaeffle, S., Kaiser, J., Büchler, M.W., Hackert, T.: The sendai and fukuoka consensus criteria for the management of branch duct ipmn-a meta-analysis on their accuracy. *Pancreatology* **17**(2), 255–262 (2017)
- [10] Gonda, T.A., Cahen, D.L., Farrell, J.J.: Pancreatic cysts. *New England Journal of Medicine* **391**(9), 832–843 (2024)
- [11] Robles, E.P.-C., Maire, F., Cros, J., Vullierme, M.-P., Rebours, V., Sauvanet, A.,

- Aubert, A., Dokmak, S., Lévy, P., Ruszniewski, P.: Accuracy of 2012 international consensus guidelines for the prediction of malignancy of branch-duct intraductal papillary mucinous neoplasms of the pancreas. *United European Gastroenterology Journal* **4**(4), 580–586 (2016)
- [12] Maggi, G., Guarneri, G., Gasparini, G., Fogliati, A., Partelli, S., Falconi, M., Crippa, S.: Pancreatic cystic neoplasms: What is the most cost-effective follow-up strategy? *Endoscopic Ultrasound* **7**(5), 319–322 (2018)
 - [13] Bulcke, A.V., Jaekers, J., Topal, H., Vanbeckevoort, D., Vandecaveye, V., Roskams, T., Weynand, B., Dekervel, J., Van Cutsem, E., Malenstein, H., et al.: Evaluating the accuracy of three international guidelines in identifying the risk of malignancy in pancreatic cysts: a retrospective analysis of a surgical treated population. *Acta gastro-enterologica Belgica* **84** (2021)
 - [14] Romutis, S., Brand, R.: Burden of new pancreatic cyst diagnosis. *Gastrointestinal Endoscopy Clinics* **33**(3), 487–495 (2023)
 - [15] Vege, S.S., Ziring, B., Jain, R., Moayyedi, P., Adams, M.A., Dorn, S.D., Dudley-Brown, S.L., Flamm, S.L., Gellad, Z.F., Gruss, C.B., et al.: American gastroenterological association institute guideline on the diagnosis and management of asymptomatic neoplastic pancreatic cysts. *Gastroenterology* **148**(4), 819–822 (2015)
 - [16] Pancreas, E.S.G., et al.: European evidence-based guidelines on pancreatic cystic neoplasms. *Gut* **67**(5), 789–804 (2018)
 - [17] Roth, H.R., Lu, L., Farag, A., Shin, H.-C., Liu, J., Turkbey, E.B., Summers, R.M.: Deeporgan: Multi-level deep convolutional networks for automated pancreas segmentation. In: *International Conference on Medical Image Computing and Computer-assisted Intervention*, pp. 556–564 (2015). Springer
 - [18] Act, A., et al.: Health insurance portability and accountability act of 1996. *Public law* **104**, 191 (1996)
 - [19] Regulation, P.: Regulation (eu) 2016/679 of the european parliament and of the council. *Regulation (eu)* **679**(2016), 10–13 (2016)
 - [20] Zhang, Z., Yao, L., Keles, E., Velichko, Y., Bagci, U.: Deep learning algorithms for pancreas segmentation from radiology scans: A review. *Advances in Clinical Radiology* **5**(1), 31–52 (2023)
 - [21] Cai, J., Lu, L., Xie, Y., Xing, F., Yang, L.: Improving deep pancreas segmentation in ct and mri images via recurrent neural contextual learning and direct loss function. *arXiv preprint arXiv:1707.04912* (2017)

- [22] Proietto Salanitri, F., Bellitto, G., Irmakci, I., Palazzo, S., Bagci, U., Spampinato, C.: Hierarchical 3d feature learning for pancreas segmentation. In: Machine Learning in Medical Imaging: 12th International Workshop, MLMI 2021, Held in Conjunction with MICCAI 2021, Strasbourg, France, September 27, 2021, Proceedings 12, pp. 238–247 (2021)
- [23] Zhang, Z., Keles, E., Durak, G., Taktak, Y., Susladkar, O., Gorade, V., Jha, D., Ormeci, A.C., Medetalibeyoglu, A., Yao, L., *et al.*: Large-scale multi-center ct and mri segmentation of pancreas with deep learning. *Medical image analysis* **99**, 103382 (2025)
- [24] Chakraborty, J., Midya, A., Gazit, L., Attiyeh, M., Langdon-Embry, L., Allen, P.J., Do, R.K., Simpson, A.L.: Ct radiomics to predict high-risk intraductal papillary mucinous neoplasms of the pancreas. *Medical physics* **45**(11), 5019–5029 (2018)
- [25] Cui, S., Tang, T., Su, Q., Wang, Y., Shu, Z., Yang, W., Gong, X.: Radiomic nomogram based on mri to predict grade of branching type intraductal papillary mucinous neoplasms of the pancreas: a multicenter study. *Cancer Imaging* **21**(1), 26 (2021)
- [26] Hussein, S., Kandel, P., Corral, J.E., Bolan, C.W., Wallace, M.B., Bagci, U.: Deep multi-modal classification of intraductal papillary mucinous neoplasms (ipmn) with canonical correlation analysis. In: 2018 IEEE 15th International Symposium on Biomedical Imaging (ISBI 2018), pp. 800–804 (2018). IEEE
- [27] LaLonde, R., Tanner, I., Nikiforaki, K., Papadakis, G.Z., Kandel, P., Bolan, C.W., Wallace, M.B., Bagci, U.: Inn: inflated neural networks for ipmn diagnosis. In: International Conference on Medical Image Computing and Computer-Assisted Intervention, pp. 101–109 (2019). Springer
- [28] Salanitri, F.P., Bellitto, G., Palazzo, S., Irmakci, I., Wallace, M., Bolan, C., Engels, M., Hoogenboom, S., Aldinucci, M., Bagci, U., *et al.*: Neural transformers for intraductal papillary mucosal neoplasms (ipmn) classification in mri images. In: 2022 44th Annual International Conference of the IEEE Engineering in Medicine & Biology Society (EMBC), pp. 475–479 (2022). IEEE
- [29] Yao, L., Zhang, Z., Demir, U., Keles, E., Vendrami, C., Agarunov, E., Bolan, C., Schoots, I., Bruno, M., Keswani, R., *et al.*: Radiomics boosts deep learning model for ipmn classification. In: International Workshop on Machine Learning in Medical Imaging, pp. 134–143 (2023). Springer
- [30] Hatamizadeh, A., Nath, V., Tang, Y., Yang, D., Roth, H.R., Xu, D.: Swin unetr: Swin transformers for semantic segmentation of brain tumors in mri images. In: Proceedings of the International MICCAI Brainlesion Workshop, pp. 272–284 (2021)

- [31] Huang, G., Liu, Z., Van Der Maaten, L., Weinberger, K.Q.: Densely connected convolutional networks. In: Proceedings of the IEEE Conference on Computer Vision and Pattern Recognition, pp. 4700–4708 (2017)
- [32] Zhang, Z., Bagci, U.: Dynamic linear transformer for 3d biomedical image segmentation. In: International Workshop on Machine Learning in Medical Imaging, pp. 171–180 (2022). Springer
- [33] Isensee, F., Jaeger, P.F., Kohl, S.A., Petersen, J., Maier-Hein, K.H.: nnu-net: a self-configuring method for deep learning-based biomedical image segmentation. *Nature methods* **18**(2), 203–211 (2021)
- [34] Selvaraju, R.R., Cogswell, M., Das, A., Vedantam, R., Parikh, D., Batra, D.: Grad-cam: Visual explanations from deep networks via gradient-based localization. In: Proceedings of the IEEE International Conference on Computer Vision, pp. 618–626 (2017)
- [35] Schulz, K., Sixt, L., Tombari, F., Landgraf, T.: Restricting the flow: Information bottlenecks for attribution. *arXiv preprint arXiv:2001.00396* (2020)
- [36] Demir, U., Irmakci, I., Keles, E., Topcu, A., Xu, Z., Spampinato, C., Jambawalikar, S., Turkbey, E., Turkbey, B., Bagci, U.: Information bottleneck attribution for visual explanations of diagnosis and prognosis. In: International Workshop on Machine Learning in Medical Imaging, pp. 396–405 (2021). Springer
- [37] McMahan, B., Moore, E., Ramage, D., Hampson, S., Arcas, B.A.: Communication-efficient learning of deep networks from decentralized data. In: Artificial Intelligence and Statistics, pp. 1273–1282 (2017). PMLR
- [38] Li, T., Sahu, A.K., Zaheer, M., Sanjabi, M., Talwalkar, A., Smith, V.: Federated optimization in heterogeneous networks. *Proceedings of Machine learning and systems* **2**, 429–450 (2020)
- [39] Wang, H., Yurochkin, M., Sun, Y., Papailiopoulos, D., Khazaeni, Y.: Federated learning with matched averaging. *arXiv preprint arXiv:2002.06440* (2020)
- [40] Peng, X., Huang, Z., Zhu, Y., Saenko, K.: Federated adversarial domain adaptation. *arXiv preprint arXiv:1911.02054* (2019)
- [41] Yao, C.-H., Gong, B., Qi, H., Cui, Y., Zhu, Y., Yang, M.-H.: Federated multi-target domain adaptation. In: Proceedings of the IEEE/CVF Winter Conference on Applications of Computer Vision, pp. 1424–1433 (2022)
- [42] Liu, Q., Chen, C., Qin, J., Dou, Q., Heng, P.-A.: Feddg: Federated domain generalization on medical image segmentation via episodic learning in continuous frequency space. In: Proceedings of the IEEE/CVF Conference on Computer Vision and Pattern Recognition, pp. 1013–1023 (2021)

- [43] Zhang, R., Xu, Q., Yao, J., Zhang, Y., Tian, Q., Wang, Y.: Federated domain generalization with generalization adjustment. In: Proceedings of the IEEE/CVF Conference on Computer Vision and Pattern Recognition, pp. 3954–3963 (2023)
- [44] Pan, H., Wang, B., Zhang, Z., Zhu, X., Jha, D., Cetin, A.E., Spampinato, C., Bagci, U.: Domain generalization with fourier transform and soft thresholding. In: ICASSP 2024-2024 IEEE International Conference on Acoustics, Speech and Signal Processing (ICASSP), pp. 2106–2110 (2024). IEEE
- [45] Pan, H., Jha, D., Biswas, K., Bagci, U.: Frequency-based federated domain generalization for polyp segmentation. In: ICASSP 2025-2025 IEEE International Conference on Acoustics, Speech and Signal Processing (ICASSP), pp. 1–5 (2025). IEEE
- [46] Kassem, H., Alapatt, D., Mascagni, P., Karargyris, A., Padoy, N.: Federated cycling (fedcy): Semi-supervised federated learning of surgical phases. *IEEE transactions on medical imaging* **42**(7), 1920–1931 (2022)
- [47] Geyer, R.C., Klein, T., Nabi, M.: Differentially private federated learning: A client level perspective. *arXiv preprint arXiv:1712.07557* (2017)
- [48] Cheng, A., Wang, P., Zhang, X.S., Cheng, J.: Differentially private federated learning with local regularization and sparsification. In: Proceedings of the IEEE/CVF Conference on Computer Vision and Pattern Recognition, pp. 10122–10131 (2022)
- [49] Bonawitz, K., Ivanov, V., Kreuter, B., Marcedone, A., McMahan, H.B., Patel, S., Ramage, D., Segal, A., Seth, K.: Practical secure aggregation for privacy-preserving machine learning. In: Proceedings of the 2017 ACM SIGSAC Conference on Computer and Communications Security, pp. 1175–1191 (2017)
- [50] Sadri, A.R., Janowczyk, A., Zhou, R., Verma, R., Beig, N., Antunes, J., Madabhushi, A., Tiwari, P., Viswanath, S.E.: Mrqy—an open-source tool for quality control of mr imaging data. *Medical physics* **47**(12), 6029–6038 (2020)
- [51] Yushkevich, P.A., Gao, Y., Gerig, G.: Itk-snap: An interactive tool for semi-automatic segmentation of multi-modality biomedical images. In: Proceedings of the 2016 38th Annual International Conference of the IEEE Engineering in Medicine and Biology Society (EMBC), pp. 3342–3345 (2016)
- [52] Shen, Z., Zhang, M., Zhao, H., Yi, S., Li, H.: Efficient attention: Attention with linear complexities. In: Proceedings of the IEEE/CVF Winter Conference on Applications of Computer Vision, pp. 3531–3539 (2021)
- [53] Paszke, A., Gross, S., Massa, F., Lerer, A., Bradbury, J., Chanan, G., Killeen, T., Lin, Z., Gimelshein, N., Antiga, L., et al.: Pytorch: An imperative style, high-performance deep learning library. *Advances in neural information processing*

- [54] Cardoso, M.J., Li, W., Brown, R., Ma, N., Kerfoot, E., Wang, Y., Murrey, B., Myronenko, A., Zhao, C., Yang, D., et al.: Monai: An open-source framework for deep learning in healthcare. arXiv preprint arXiv:2211.02701 (2022)
- [55] Malik, J., Belongie, S., Leung, T., Shi, J.: Contour and texture analysis for image segmentation. *International journal of computer vision* **43**(1), 7–27 (2001)
- [56] Haralick, R.M., Shanmugam, K., Dinstein, I.H.: Textural features for image classification. *IEEE Transactions on systems, man, and cybernetics* (6), 610–621 (2007)
- [57] Prasanna, P., Tiwari, P., Madabhushi, A.: Co-occurrence of local anisotropic gradient orientations (collage): a new radiomics descriptor. *Scientific reports* **6**(1), 37241 (2016)
- [58] Peng, H., Long, F., Ding, C.: Feature selection based on mutual information criteria of max-dependency, max-relevance, and min-redundancy. *IEEE Transactions on pattern analysis and machine intelligence* **27**(8), 1226–1238 (2005)
- [59] Ho, T.K.: Random decision forests. In: *Proceedings of 3rd International Conference on Document Analysis and Recognition*, vol. 1, pp. 278–282 (1995). IEEE
- [60] Loshchilov, I.: Decoupled weight decay regularization. arXiv preprint arXiv:1711.05101 (2017)
- [61] He, K., Zhang, X., Ren, S., Sun, J.: Deep residual learning for image recognition. In: *Proceedings of the IEEE Conference on Computer Vision and Pattern Recognition*, pp. 770–778 (2016)
- [62] Hara, K., Kataoka, H., Satoh, Y.: Can spatiotemporal 3d cnns retrace the history of 2d cnns and imagenet? In: *Proceedings of the IEEE Conference on Computer Vision and Pattern Recognition*, pp. 6546–6555 (2018)
- [63] Ma, N., Zhang, X., Zheng, H.-T., Sun, J.: Shufflenet v2: Practical guidelines for efficient cnn architecture design. In: *Proceedings of the European Conference on Computer Vision (ECCV)*, pp. 116–131 (2018)
- [64] Sandler, M., Howard, A., Zhu, M., Zhmoginov, A., Chen, L.-C.: Mobilenetv2: Inverted residuals and linear bottlenecks. In: *Proceedings of the IEEE Conference on Computer Vision and Pattern Recognition*, pp. 4510–4520 (2018)
- [65] Tan, M., Le, Q.: Efficientnet: Rethinking model scaling for convolutional neural networks. In: *International Conference on Machine Learning*, pp. 6105–6114 (2019). PMLR

Appendix A Supplementary Materials

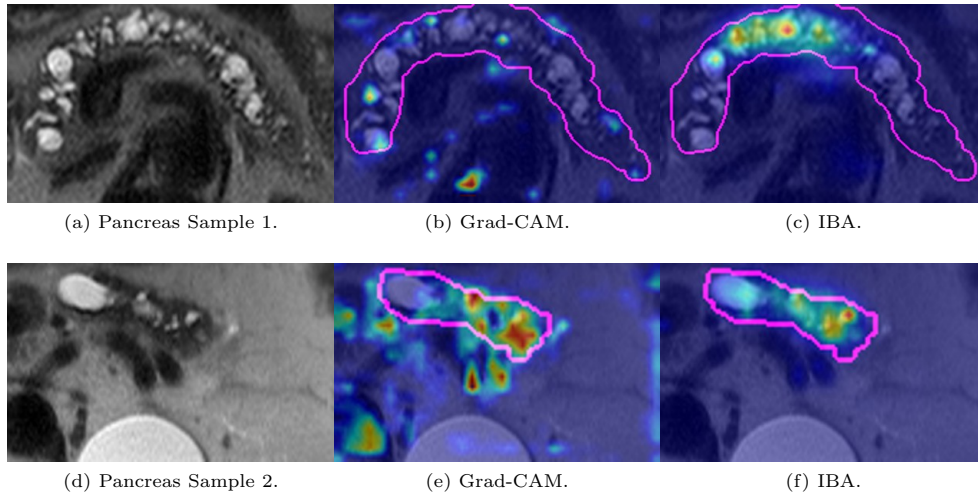


Fig. A1: Visual explanations using Grad-CAM and IBA.

Table A1: Data Distribution for IPMN Classification.

Data Centers	T1W Modality				T2W Modality			
	No Risk	Low Risk	High Risk	Total	No Risk	Low Risk	High Risk	Total
Center 1: NYU	48	79	23	150	48	79	24	151
Center 2: MCF	29	42	63	134	25	42	63	130
Center 3: NU	43	126	17	186	44	127	16	187
Center 4: AHN	1	11	4	16	1	13	4	18
Center 5: MCA	0	10	14	24	0	7	16	23
Center 6: IU	3	48	13	64	3	46	14	63
Center 7: EMC	40	23	15	78	38	30	15	83
Total	164	339	149	652	159	344	152	655

Table A2: PanSegNet’s performance

Center	Dice(%)	Jaccard(%)	Precision(%)	Recall(%)	HD95(mm)	ASSD(mm)
T1W Modality						
NYU	84.99±7.74	74.56±9.84	84.80±8.66	86.10±8.32	5.96±5.31	1.26±1.19
MCF	87.47±5.79	78.17±8.37	87.63±7.44	88.11±7.37	5.35±5.68	1.07±0.94
NU	88.33±5.89	79.52±7.98	87.49±7.69	89.72±5.74	4.53±6.86	1.15±0.89
AHN	81.22±6.11	68.79±8.16	84.54±8.92	79.15±7.85	8.27±3.75	1.61±0.78
MCA	78.72±10.98	66.03±12.55	75.29±14.90	85.04±6.52	8.37±10.79	2.04±2.21
IU	85.37±9.91	75.56±12.65	86.13±9.51	85.54±11.58	8.65±16.96	1.89±2.72
EMC	89.96±4.06	81.98±6.16	89.64±5.01	90.53±4.89	5.67±21.28	1.33±2.30
Global	86.81±7.30	77.32±9.74	86.56±8.59	87.84±7.80	5.81±10.90	1.30±1.55
T2W Modality						
NYU	87.17±4.39	77.52±6.62	87.98±6.22	86.88±6.16	5.03±3.17	0.93±0.49
MCF	87.85±5.58	78.72±7.86	89.13±6.01	87.34±8.02	4.94±6.61	0.96±1.13
NU	92.50±5.15	86.41±7.81	92.43±5.85	92.91±5.94	2.94±3.25	0.52±0.63
AHN	82.72±9.25	71.46±11.73	86.60±11.08	80.15±9.62	7.16±6.41	1.33±1.45
MCA	84.84±3.27	73.82±4.92	87.38±5.91	83.12±6.51	6.18±3.60	0.99±0.46
IU	92.46±3.73	86.19±6.18	94.16±4.17	91.02±5.06	2.46±1.97	0.40±0.28
EMC	91.05±8.64	84.46±11.30	93.38±4.78	89.74±11.02	4.39±7.38	0.70±1.18
Global	89.62±6.38	81.73±9.31	90.74±6.45	89.11±8.06	4.19±4.99	0.75±0.87

Table A3: Swin-UNETR’s performance

Center	Dice(%)	Jaccard(%)	Precision(%)	Recall(%)	HD95(mm)	ASSD(mm)
T1W Modality						
NYU	77.78±2.40	65.26±2.51	77.48±3.78	80.72±1.68	23.76±11.55	6.93±5.58
MCF	81.63±2.92	70.17±3.51	82.97±2.06	82.05±3.48	11.27±2.84	2.68±1.71
NU	82.89±2.06	72.00±2.89	82.21±2.55	84.90±1.77	13.77±4.98	3.34±0.96
AHN	65.14±11.05	50.90±10.48	74.43±6.51	61.04±12.47	22.51±15.68	4.23±2.94
MCA	67.50±6.05	52.45±6.56	66.26±4.72	70.99±7.94	63.22±28.78	13.67±6.59
IU	79.17±2.31	67.09±3.06	78.74±3.73	81.87±3.43	30.53±6.75	8.03±2.95
EMC	74.30±2.49	61.89±3.31	73.22±5.13	79.46±2.72	72.44±48.10	24.83±19.55
Global	79.09±1.40	67.19±1.63	79.09±1.67	81.37±0.74	26.55±8.48	7.58±3.76
T2W Modality						
NYU	78.81±1.67	66.10±2.09	80.73±2.84	78.61±2.42	13.21±2.28	2.72±0.89
MCF	79.43±2.06	67.22±2.50	83.70±2.83	77.72±1.45	13.06±2.93	1.75±0.26
NU	81.18±1.02	69.80±1.04	81.48±0.04	82.19±1.95	17.38±3.96	4.20±1.52
AHN	64.21±6.26	50.03±6.59	72.19±8.17	64.18±9.03	31.07±13.51	8.69±5.93
MCA	59.63±4.03	44.37±3.81	63.87±5.44	61.36±9.01	81.04±22.10	24.77±8.46
IU	78.47±1.47	65.74±2.06	81.70±2.05	76.57±3.74	23.25±11.22	3.77±1.91
EMC	63.39±5.87	49.69±5.98	65.73±8.97	69.20±5.54	87.79±40.81	28.59±14.81
Global	76.29±0.66	63.77±0.82	78.70±2.14	76.86±1.21	28.53±7.01	7.57±2.60

Table A4: Swin-UNETR+FedAvg’s performance

Center	Dice(%)	Jaccard(%)	Precision(%)	Recall(%)	HD95(mm)	ASSD(mm)
T1W Modality						
NYU	71.84±2.51	58.25±2.21	71.06±3.45	76.67±1.26	34.81±8.00	12.12±6.18
MCF	77.94±3.36	65.40±3.85	79.16±3.10	79.07±3.57	15.64±3.96	3.60±1.74
NU	77.61±2.78	65.25±3.38	74.06±2.82	83.66±1.95	31.89±5.17	8.36±1.83
AHN	51.07±10.96	37.61±8.85	61.60±4.80	48.41±13.08	34.78±12.52	12.68±8.57
MCA	46.13±11.55	32.28±10.35	40.38±10.29	59.55±12.69	110.16±36.15	44.79±18.87
IU	71.09±3.26	58.03±4.01	67.60±3.86	80.11±4.29	53.95±6.37	15.16±3.77
EMC	55.67±8.40	42.23±8.18	53.61±11.02	67.57±0.69	106.46±50.34	43.83±26.68
Global	71.26±2.59	58.30±2.74	69.74±3.09	77.13±1.34	43.65±8.60	14.77±5.01
T2W Modality						
NYU	74.35±1.48	60.40±1.65	76.41±3.60	74.20±2.62	23.85±7.88	5.02±2.26
MCF	74.69±2.19	61.36±2.24	80.06±3.04	72.72±1.71	15.10±2.44	2.64±0.62
NU	73.99±2.16	60.71±2.15	73.26±2.12	76.54±2.20	27.46±2.41	6.97±1.70
AHN	59.41±4.71	45.24±3.78	64.31±3.14	60.20±6.89	43.94±7.98	15.80±5.17
MCA	43.20±4.86	29.99±3.94	40.48±4.54	55.05±8.71	129.24±14.32	46.21±10.93
IU	65.74±3.60	51.15±3.71	66.98±4.91	67.52±3.44	59.26±14.00	13.29±4.07
EMC	54.50±7.95	40.46±7.54	53.28±10.43	63.44±5.58	104.14±30.44	34.60±14.15
Global	69.19±1.51	55.48±1.44	70.52±2.98	71.31±0.95	41.87±5.84	11.74±3.02

Table A5: Swin-UNETR+FedProx($\mu = 0.3$)’s performance

Center	Dice(%)	Jaccard(%)	Precision(%)	Recall(%)	HD95(mm)	ASSD(mm)
T1W Modality						
NYU	60.31±2.27	46.02±2.12	59.92±2.67	66.25±0.97	81.99±9.69	26.72±5.39
MCF	71.63±4.18	57.63±4.54	73.65±4.55	72.56±3.43	30.03±11.76	6.65±3.25
NU	65.07±3.77	51.06±3.74	62.81±4.73	70.57±2.54	91.69±8.79	24.60±3.51
AHN	36.24±10.71	24.91±8.01	37.94±9.71	38.25±13.66	101.79±4.39	35.16±10.74
MCA	26.91±15.07	18.28±11.69	23.06±13.27	41.17±16.93	141.22±30.07	74.43±24.62
IU	49.87±5.22	36.51±4.64	43.31±5.09	64.78±6.79	123.78±8.26	47.66±5.68
EMC	28.87±14.46	20.21±10.66	34.43±19.59	33.06±13.66	132.43±43.78	74.32±36.88
Global	57.24±3.41	44.16±2.85	56.85±4.33	62.93±2.80	87.27±8.34	31.99±6.19
T2W Modality						
NYU	66.32±1.57	51.23±1.45	68.43±3.06	66.90±3.30	41.34±6.78	9.66±2.52
MCF	66.00±3.16	51.19±3.06	73.18±4.34	63.36±3.00	31.08±4.63	6.04±1.30
NU	62.60±3.64	47.76±3.39	60.81±4.80	67.36±2.27	57.78±11.94	15.84±4.55
AHN	52.45±8.06	38.52±7.26	55.24±7.96	55.00±7.23	54.94±14.03	18.18±8.25
MCA	30.01±5.61	18.73±4.48	25.81±5.46	44.53±9.74	162.60±17.22	64.85±10.62
IU	52.23±2.97	38.08±3.03	50.30±3.28	58.34±3.88	90.75±7.97	27.16±3.23
EMC	37.09±11.12	25.26±8.83	35.36±12.71	46.12±10.80	138.44±27.07	55.54±20.05
Global	58.11±2.61	43.85±2.22	59.01±4.38	61.46±1.11	66.68±9.10	20.87±4.81

Table A6: Swin-UNETR+FedProx($\mu = 0.01$)’s performance

Center	Dice(%)	Jaccard(%)	Precision(%)	Recall(%)	HD95(mm)	ASSD(mm)
T1W Modality						
NYU	70.16±2.67	56.32±2.50	68.93±2.96	75.42±1.94	48.86±6.08	15.39±5.71
MCF	77.56±3.35	64.78±3.86	78.55±2.42	78.98±4.17	16.27±5.43	3.90±1.93
NU	76.02±3.38	63.70±4.09	72.70±4.04	82.47±2.04	38.92±12.04	10.19±2.66
AHN	47.10±10.95	33.87±8.76	57.15±7.38	44.02±13.92	48.54±16.35	17.19±9.42
MCA	38.75±13.79	26.78±11.58	33.39±12.75	52.80±14.80	118.66±40.33	58.79±22.81
IU	67.67±3.76	54.48±4.85	64.12±4.80	77.69±4.72	70.14±9.79	21.67±4.17
EMC	50.07±12.37	37.68±11.39	47.84±14.68	61.21±7.92	119.22±48.27	55.12±31.83
Global	68.95±3.30	56.09±3.37	67.33±3.37	75.11±2.68	52.82±9.97	18.76±5.41
T2W Modality						
NYU	73.58±1.54	59.53±1.75	75.26±3.12	74.01±2.91	24.61±7.36	6.05±2.33
MCF	73.70±2.45	60.23±2.54	78.80±2.98	71.85±2.17	18.39±4.02	3.23±0.79
NU	72.90±2.49	59.35±2.47	71.49±1.54	76.13±3.82	31.58±4.63	8.19±1.97
AHN	57.18±7.15	43.33±5.93	65.22±8.08	59.25±10.56	53.58±13.61	16.15±7.26
MCA	39.65±4.32	26.78±3.34	35.97±4.44	52.74±7.16	143.75±17.54	53.97±13.63
IU	62.72±2.67	47.93±2.82	63.94±3.16	65.58±3.93	70.23±10.51	16.80±3.20
EMC	48.97±7.65	35.23±6.79	46.97±11.17	60.22±3.52	122.75±28.92	45.19±15.92
Global	67.25±1.86	53.47±1.77	68.22±2.99	70.23±1.21	48.36±6.51	14.52±3.64

Table A7: Swin-UNETR+FedProx($\mu = 0.005$)’s performance

Center	Dice(%)	Jaccard(%)	Precision(%)	Recall(%)	HD95(mm)	ASSD(mm)
T1W Modality						
NYU	70.36±2.53	56.56±2.52	69.05±3.13	75.88±1.13	45.50±9.37	14.81±5.80
MCF	78.06±3.01	65.45±3.43	78.71±2.11	79.71±3.99	16.84±4.69	3.89±1.76
NU	77.12±3.06	64.79±3.77	73.90±3.36	83.19±2.12	34.39±8.18	8.86±2.00
AHN	49.40±10.96	36.07±8.83	58.90±8.21	46.13±12.58	44.40±25.11	14.65±9.00
MCA	41.21±13.62	28.85±11.78	37.23±12.92	54.25±14.72	118.45±41.69	53.98±23.47
IU	68.46±3.17	55.10±3.98	64.54±3.92	77.89±4.16	62.72±7.43	19.55±3.45
EMC	51.19±11.52	38.50±10.66	49.55±13.78	62.32±6.74	116.00±50.94	52.80±31.64
Global	69.77±2.90	56.88±2.98	68.16±2.98	75.82±2.39	49.61±8.55	17.51±5.39
T2W Modality						
NYU	73.95±1.71	59.96±1.95	75.27±2.96	74.70±2.76	23.38±6.26	5.50±1.87
MCF	74.07±2.93	60.69±2.97	79.08±3.05	72.32±2.92	17.86±3.41	3.12±0.79
NU	73.45±2.47	60.05±2.53	71.86±1.80	77.06±3.60	35.49±4.63	8.57±1.95
AHN	56.13±5.71	42.54±4.85	60.49±4.12	57.76±8.25	44.34±11.90	16.72±5.56
MCA	41.39±5.59	28.18±4.58	37.43±5.67	54.20±8.71	138.35±23.02	48.29±13.09
IU	63.61±1.86	49.21±2.25	65.14±2.76	65.75±3.16	69.52±11.55	16.15±2.49
EMC	50.03±8.99	36.43±8.09	48.70±11.38	61.28±4.41	123.65±25.87	43.32±15.18
Global	67.82±1.44	54.16±1.43	68.63±2.41	70.89±0.84	48.64±5.82	13.99±2.96

Table A8: Binary Classification (High Risk or Not) Results for Multi-Center IPMN MRI Using DenseNet-121.

Method	T1W Modality		T2W Modality	
	ACC(%)	AUC(%)	ACC(%)	AUC(%)
Center 1: New York University Langone Health (NYU)				
Centralized	86.65±3.37	77.09±12.25	83.50±7.70	87.54±3.89
FedAvg	81.28±4.45	68.42±13.05	87.43±2.12	90.05±4.79
FedProx ($\mu = 0.1$)	81.95±5.31	68.92±14.56	85.40±3.11	88.98±5.36
FedProx ($\mu = 0.3$)	73.19±15.91	70.19±14.82	86.79±3.14	92.67±3.60
Center 2: Mayo Clinic Florida (MCF)				
Centralized	65.71±8.49	74.80±13.04	72.44±12.66	81.46±10.11
FedAvg	64.95±9.86	74.31±10.05	70.79±4.94	80.85±8.25
FedProx ($\mu = 0.1$)	65.75±11.13	73.66±12.14	67.80±8.71	80.75±9.88
FedProx ($\mu = 0.3$)	65.02±13.48	74.94±13.22	63.87±10.16	81.10±6.57
Center 3: Northwestern University (NU)				
Centralized	84.96±5.82	67.66±10.41	82.93±9.11	57.34±16.99
FedAvg	90.33±2.36	74.66±13.61	90.89±2.43	57.94±17.95
FedProx ($\mu = 0.1$)	88.15±2.52	73.46±10.93	84.93±10.16	60.18±22.42
FedProx ($\mu = 0.3$)	88.16±2.46	73.54±14.27	89.29±2.20	58.24±27.04
Center 4: Allegheny Health Network (AHN)				
Centralized	87.50±12.50	66.67±40.82	67.50±19.20	70.83±29.76
FedAvg	50.00±17.68	33.33±23.57	76.25±17.81	85.42±14.88
FedProx ($\mu = 0.1$)	56.25±32.48	58.33±43.30	70.00±27.61	70.83±18.16
FedProx ($\mu = 0.3$)	56.25±36.98	58.33±36.32	88.75±11.39	79.17±21.65
Center 5: Mayo Clinic Arizona (MCA)				
Centralized	66.67±20.41	73.26±23.88	55.00±20.21	75.00±25.00
FedAvg	75.00±14.43	85.07±15.88	48.33±9.57	75.00±15.31
FedProx ($\mu = 0.1$)	75.00±14.43	88.19±11.85	44.17±11.40	68.75±27.24
FedProx ($\mu = 0.3$)	62.50±13.82	88.19±11.85	39.17±6.82	81.25±10.83
Center 6: Istanbul University Faculty of Medicine (IU)				
Centralized	78.12±6.99	64.50±24.95	79.48±4.87	83.36±11.06
FedAvg	79.69±5.18	63.02±20.20	76.35±9.00	78.79±13.25
FedProx ($\mu = 0.1$)	75.00±7.65	59.46±20.63	79.58±9.09	77.42±13.58
FedProx ($\mu = 0.3$)	70.31±19.45	62.54±16.40	77.81±2.85	79.86±11.47
Center 7: Erasmus Medical Center (EMC)				
Centralized	83.22±7.76	84.45±7.30	74.82±13.06	83.95±11.71
FedAvg	80.79±2.02	66.87±17.54	77.20±11.72	68.75±12.10
FedProx ($\mu = 0.1$)	79.47±3.76	83.31±15.08	77.20±6.84	81.74±16.10
FedProx ($\mu = 0.3$)	78.16±2.62	81.12±15.36	77.14±6.06	78.68±11.32
Global				
Centralized	79.90±1.52	78.13±2.06	78.23±5.09	82.37±1.02
FedAvg	79.29±2.04	76.19±1.02	81.08±1.69	81.24±2.98
FedProx ($\mu = 0.1$)	78.52±1.23	76.46±1.21	78.29±2.87	81.35±1.77
FedProx ($\mu = 0.3$)	75.26±4.90	76.67±1.09	79.27±2.41	81.81±2.15

Table A9: Comparison of IPMN Classification Accuracy: Radiologists vs. DenseNet-121.

Method	Input Modality		Three-Class Classification			Binary Classification	
	T1W	T2W	No-Risk	Low-Risk	High-Risk	No/Low-Risk	High-Risk
Radiologist 1	✓	✓	89.03	58.43	64.08	89.94	64.08
Radiologist 2	✓	✓	93.55	30.12	32.39	97.13	32.39
Radiologist 3	✓	✓	91.61	56.33	41.55	94.66	41.55
Average	✓	✓	91.40	48.29	46.01	93.91	46.01
DenseNet-121	✓	✗	37.42	81.02	33.80	91.38	40.85
DenseNet-121	✗	✓	54.55	79.13	52.52	86.11	53.96
DenseNet-121(feature fusion)	✓	✓	45.16	83.13	42.96	95.69	43.66
DenseNet-121(probability fusion)	✓	✓	45.16	84.94	45.77	94.66	47.18